

Key Points:

- Martian water ice cloud particle sizes exhibit a clear seasonal cycle
- Cloud particle sizes typically exhibit a gradient of size with height with larger particles closer to the surface
- The seasonal cycle is different at tropical latitudes relative to polar latitudes

Supporting Information:

- Supporting Information S1
- Data Set S1

Correspondence to:

S. D. Guzewich,
scott.d.guzewich@nasa.gov

Citation:

Guzewich, S. D., & Smith, M. D. (2019). Seasonal variation in Martian water ice cloud particle size. *Journal of Geophysical Research: Planets*, 124, 636–643. <https://doi.org/10.1029/2018JE005843>

Received 1 OCT 2018

Accepted 17 JAN 2019

Accepted article online 21 JAN 2019

Published online 27 FEB 2019

Seasonal Variation in Martian Water Ice Cloud Particle Size

Scott D. Guzewich¹  and M. D. Smith¹ 

¹NASA Goddard Spaceflight Center, Greenbelt, MD, USA

Abstract We employ the complete record of Mars limb-viewing observations by the Compact Reconnaissance Imaging Spectrometer for Mars, totaling 922 successful retrievals, to chart the seasonal variation in water ice cloud particle size. Low-latitude clouds exhibit particle size sorting with altitude at all seasons, with particles ranging from $>3.0\text{ }\mu\text{m}$ in effective radius to $1.0\text{--}1.5\text{ }\mu\text{m}$. However, at a given altitude, the ice particle size often varies through the year. Ice particle sizes in the tropics follow a different seasonal cycle than ice mixing ratio. North polar clouds have a complex seasonal cycle, with a sloped size profile with altitude as the polar hood cloud forms in early fall trending to a roughly uniform $1.5\text{-}\mu\text{m}$ profile by the end of winter. These data are an important metric to validate and improve general circulation model microphysical routines and to better understand how Martian water ice clouds influence the atmospheric radiative budget.

Plain Language Summary Knowledge of the size of Martian water ice cloud particles is critical to understanding how they interact radiatively with the atmosphere, and thus how they modify the temperature structure and circulation of Mars' atmosphere. The size of the particles is also important to properly and self-consistently model the Martian atmosphere with general circulation models. Here we retrieve the vertical distribution of water ice cloud particle sizes from limb-viewing observations with the Compact Reconnaissance Imaging Spectrometer for Mars and find that there is a clear seasonal cycle to the particle sizes. Additionally, the polar atmosphere and low latitudes have distinctly different seasonal cycles, suggesting different processes are at work. These data represent an important metric to guide the improvement of Mars general circulation models and to better understand Mars' atmospheric processes.

1. Introduction

Water ice clouds play an important role in modulating the current Martian climatic regime and help control many diagnostic aspects of the Martian atmosphere including temperature, atmospheric waves, and the broader circulation through their radiative properties (Kahre et al., 2015; Montmessin et al., 2004; Mulholland et al., 2016; Pottier et al., 2017; Steele et al., 2014; Wilson & Guzewich, 2014; Wilson et al., 2008, 2007). The incorporation of water ice clouds into Mars general circulation models (GCMs) has resulted in a substantial improvement in the correlation between simulated atmospheric parameters and observations (Kahre et al., 2015; Lee et al., 2018; Madeleine et al., 2012; Navarro et al., 2014; Pottier et al., 2017; Shaposhnikov et al., 2018). Yet despite these improvements in our view of and ability to simulate the Martian atmosphere, discrepancies and unresolved questions linger. Specifically, the assimilation of observations into GCMs is reaching the limitations of both the observations and the GCM physics (e.g., Navarro et al., 2017). Additional data are needed to reduce modeling biases and guide the improvement of model physics.

Microphysical interaction between dust and water ice is one such area that has received increased focus in recent years as a possible avenue to improve Mars GCMs (Kahre et al., 2015; Lee et al., 2018; Navarro et al., 2014; Pottier et al., 2017; Shaposhnikov et al., 2018). While earlier iterations of some Mars GCMs used water ice particle size as a tuning parameter (through the changing interaction with solar radiation driven by different particle sizes), many GCMs are moving toward more self-consistent microphysical modeling of water ice particle sizes driven by factors such as abundance of cloud condensation nuclei and water vapor partial pressure (Lee et al., 2018). These microphysical routines track the evolution of water ice cloud particle size distributions through time and space.

In this work, we present the seasonal evolution and variability of the vertical distribution of Martian water ice cloud particle size (specifically, effective radius [r_{eff}]) as observed by the Compact Reconnaissance

Imaging Spectrometer for Mars (CRISM) in limb-scanning mode. This work extends the analysis presented by Guzewich et al. (2014). These observations represent an important metric to evaluate the performance of Mars GCM microphysical modules and guide their improvement while also providing a window into Martian atmospheric aerosol interactions and processes.

2. Methodology

This work was enabled through CRISM (Murchie et al., 2007) limb-viewing observations, wherein the Mars Reconnaissance Orbiter spacecraft was pitched to allow CRISM to view and scan the limb of the planet (Guzewich et al., 2014; Smith et al., 2013). Due to the failure of the CRISM cryocooler (well past its design lifetime), these observations are no longer conducted. CRISM limb-viewing observations are designated with the “LMB” prefix on the Planetary Data System. Here we analyze 922 CRISM limb-viewing observations, an additional 511 beyond what was used by Guzewich et al. (2014) that were collected in Mars Years 32 and 33 (following the calendar of Clancy et al., 2000).

Thorough descriptions of the retrieval algorithm and uncertainties in the retrieved quantities are presented by Guzewich et al. (2014) and Smith et al. (2013), and the reader is referred there for additional detail. The retrieval algorithm used is identical to that employed by Guzewich et al. (2014), which is a modification of that used by Smith et al. (2013) to retrieve aerosol (dust and water ice) extinction mixing ratios ($\Delta\tau/\Delta\text{mb}$, referenced to the 2,200 nm wavelength) and effective radii and Lambert surface albedo (at each wavelength used in the retrieval) from CRISM near-infrared spectra. Retrieved values are calculated at 18 vertical levels between 0.2 and 6.6 scale heights above the surface at intervals of 0.4 scale heights (approximately 3–4 km).

We assume that water ice particles are spherical in shape and that they scatter light following Mie theory (Warren, 1984; Wiscombe, 1996). As we are fitting the effective radius, r_{eff} , we hold the effective variance of the water ice particle size distribution fixed at 0.1 following Wolff et al. (2009), Smith et al. (2013), and Guzewich et al. (2014). The retrieval is relatively insensitive to effective variance of the particle size distribution regardless. Retrievals of effective radius are only conducted when the mixing ratio is $\geq 0.09 \Delta\tau/\Delta\text{mb}$.

Following Smith et al. (2013) and Guzewich et al. (2014), we assume an uncertainty of approximately 0.1 $\Delta\tau/\Delta\text{mb}$ in water ice mixing ratio. Guzewich et al. (2014) discusses uncertainties in the retrieved effective radii in great detail. In brief, the typical water ice effective radius uncertainty half-width is near 0.1 μm above 35-km altitude and increases to approximately 0.17 μm in the lowest scale height of the atmosphere.

Note that following Petty (2006) and Kokhanovsky (2004), values of water ice opacity coupled with particle size information can be converted into water ice particle number density assuming Mie theory, as we have in our retrievals. At our reference wavelength of 2,200 nm and with water ice particles of comparable size to that wavelength, as shown below, the extinction efficiency of a spherical water ice particle (Q_e in the notation of Petty, 2006) is approximately 2.5. Hence, representative water ice mixing ratios of $\sim 0.75 \Delta\tau/\Delta\text{mb}$ at 30-km altitude in the Aphelion Cloud Belt (ACB; e.g., Figure 3) translate to a layer opacity (our retrievals are conducted in layer thicknesses of 0.4 scale heights) of approximately 0.12. Ignoring complications due to particle size distributions and differing properties of the ice nuclei (i.e., a dust grain internal to a water ice coating), this retrieved layer opacity, τ_L , is then equivalent to

$$\tau_L = Q_e A H N,$$

where A is the geometric cross-sectional area of an individual water ice particle, H is the layer thickness (in meters), and N is the water ice particle number density. This equates to a water ice particle number density of $\sim 900,000 \text{ m}^{-3}$ in this example. This is comparable to terrestrial cirrus clouds (e.g., Hoyle et al., 2005). Similarly, the same information can be used to provide water ice particle mass mixing ratio following the formula shown in Heavens et al. (2010) with a conversion factor of g , the gravitational acceleration, to convert between their opacity mixing ratio units and ours and using the density of water ice.

All CRISM retrievals used in this work are included as supporting information S1.

3. Results

The addition of another 511 CRISM limb-viewing observations allows us to complete a “monthly” (where a Mars “month” is 30° of solar longitude and we use the centered value, i.e., $L_s = 30^\circ$ represents $L_s = 15^\circ\text{--}45^\circ$)

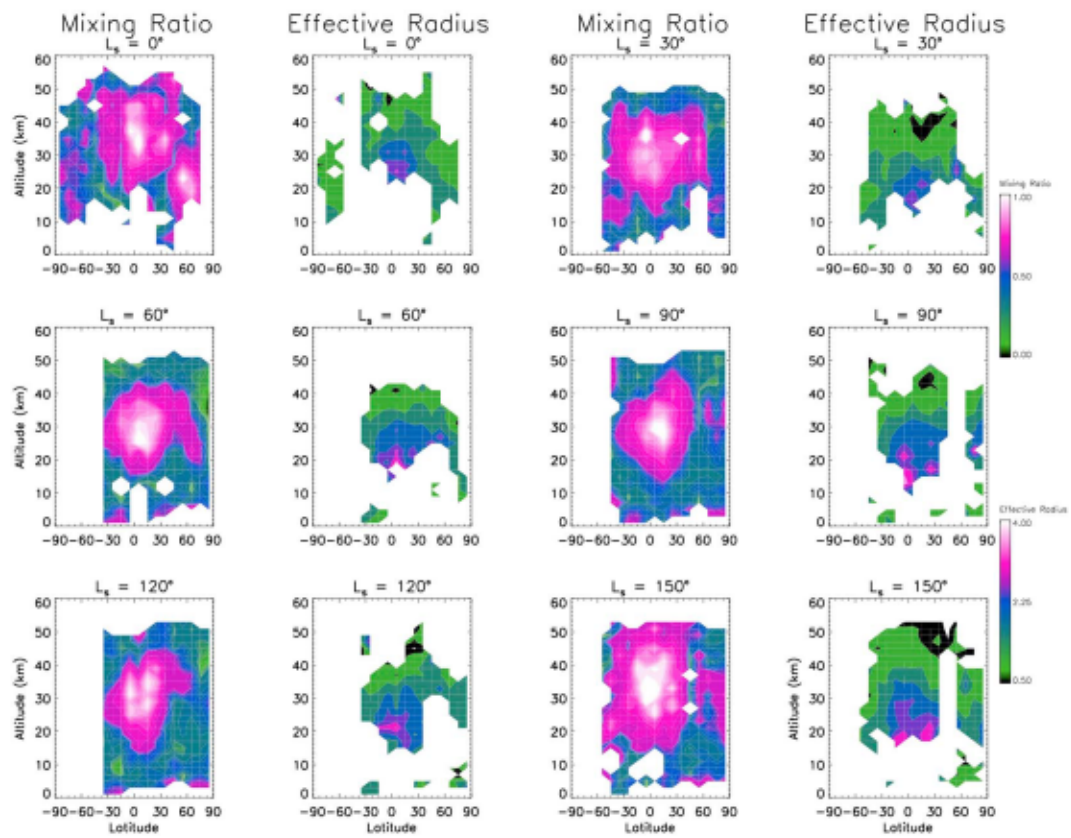


Figure 1. Zonal average Compact Reconnaissance Imaging Spectrometer for Mars water ice mixing ratio ($\Delta\tau/\Delta\text{amb}$, first and third columns) and water ice effective radius (μm) at intervals of 30° of solar longitude (centered on the listed values) for the first half of the Martian year. Note that contoured mixing ratio values saturate at $1 \Delta\tau/\Delta\text{amb}$.

climatology of water ice mixing ratio as seen in Figures 1 and 2. Note that these figures average all available data and thus represent a multiyear average. We examined the data for signs of interannual variability, but due to the sparse nature of the CRISM limb-viewing observations, we were able to make no firm conclusions. As CRISM operates in the visible and near-infrared, the observations require scattered sunlight. Hence, these observations all represent daytime (approximately 15:00 local Mars solar time based on Mars Reconnaissance Orbiter's orbital geometry) views of the atmosphere. That also excludes the polar winter atmosphere from view.

The seasonal evolution of water ice clouds in the Martian atmosphere is seen in Figures 1 and 2. Clouds are present at all times but with clear variations in their latitudinal location, altitude, and opacity based on season. Despite our limited view of the polar (winter) atmosphere with CRISM, there is still a clear delineation between tropical clouds and polar clouds in most seasons, with a band of comparatively cloud-free atmosphere between them. Figures 1 and 2 can be compared to a similar figure (Figure 17) shown by McCleese et al. (2010; also Figure 11 of Guzewich et al., 2013 showing Thermal Emission Spectrometer limb-viewing retrievals) which depicts the zonal average seasonal evolution of water ice clouds as viewed by the Mars Climate Sounder during Mars Year 29.

The evolution of the ACB at tropical latitudes (20°S – 30°N) is clear between $L_s = 30$ and 180° . The highest mixing ratios in the ACB are seen near $L_s = 150^\circ$, when they exceed $1.37 \Delta\tau/\Delta\text{amb}$ near 30–40-km altitude. The highest mixing ratios consistently occur just north of the equator (0 – 20°N) as has been seen by Pearl et al. (2001), Clancy et al. (2003), Smith (2004, 2009), and Montmessin et al. (2017; among many others). The ACB is also distinct in that the water ice layer has distinct upper and lower boundaries where the mixing ratios fall to zero or near-zero values. This is particularly true between $L_s = 30^\circ$ and 120° and was also seen by McCleese et al. (2010). After $L_s = 180^\circ$, the ACB is no longer present, and tropical clouds reach a minimum in expanse and opacity near $L_s = 240^\circ$. This timing corresponds to the typical annual peak in atmospheric

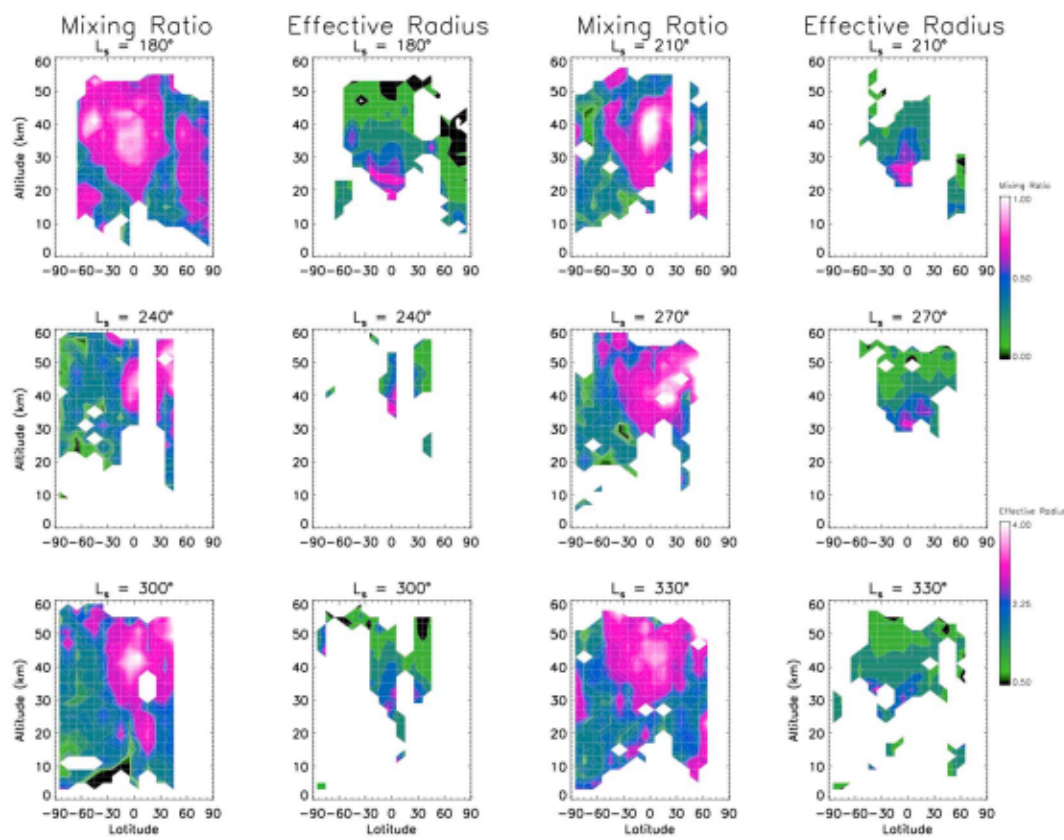


Figure 2. Same as Figure 1 except for the second half of the Martian year.

dust opacity and also when the atmosphere is often the warmest (e.g., McCleese et al., 2010; Smith, 2004, 2009). Tropical clouds then thicken as northern hemisphere winter/southern hemisphere summer progresses at higher altitudes (>40 km) above the dustier lower atmosphere. Indeed, clouds extend to higher altitudes (up to 60 km, which is the top of our retrieved altitude range) during the northern hemisphere winter/southern hemisphere summer ($L_s = 210\text{--}330^\circ$) season and cap the dustier lower atmosphere during this time of year.

Figures 1 and 2 also track the seasonal evolution of polar clouds in summer and on the latitudinal and seasonal edges of the winter polar hood clouds. In the northern hemisphere, distinct polar clouds begin forming late in summer ($L_s = 150^\circ$) poleward of 60°N at altitudes above 20 km and then thicken and extend to lower altitudes through $L_s = 210^\circ$, beyond which the north polar atmosphere is not observable. Late in northern winter ($L_s = 330^\circ$), the edge of the polar hood clouds is at low altitudes (<25 km) poleward of 45°N . The polar hood clouds then begin dissipating through early northern spring ($L_s = 30\text{--}60^\circ$), and the north polar atmosphere is nearly cloud-free during late spring and most of summer. There are fewer observations for the south polar region relative to the north polar, but the edge of the winter polar hood clouds is seen at $L_s = 180^\circ$ poleward of 45°S and below 25-km altitude. The southern hemisphere is more cloud-free in spring and summer ($L_s = 210\text{--}330^\circ$) than the northern hemisphere during its summer ($L_s = 30\text{--}150^\circ$) due to the warmer temperatures and dustier atmosphere. South polar clouds begin forming again at $L_s = 330^\circ$ above 25 km and expand in altitude and latitude coverage through the equinox at $L_s = 0^\circ$.

The monthly evolution of retrieved water ice cloud particle sizes (effective radii) is also shown in Figures 1 and 2. The sparser nature of the plotted water ice particle size data in Figures 1 and 2, relative to the mixing ratios, is due to our restriction to only retrieve water ice particle size when the mixing ratio is $\geq 0.09 \Delta r/\Delta \text{Amb}$. Guzewich et al. (2014) showed that ACB clouds exhibit a strong gradient of water ice cloud particle size with altitude, with larger particles nearer the surface and smaller particles at higher altitudes. Figures 1 and 2 show that this pattern is robust across all seasons in the middle and lower latitudes of Mars, although the

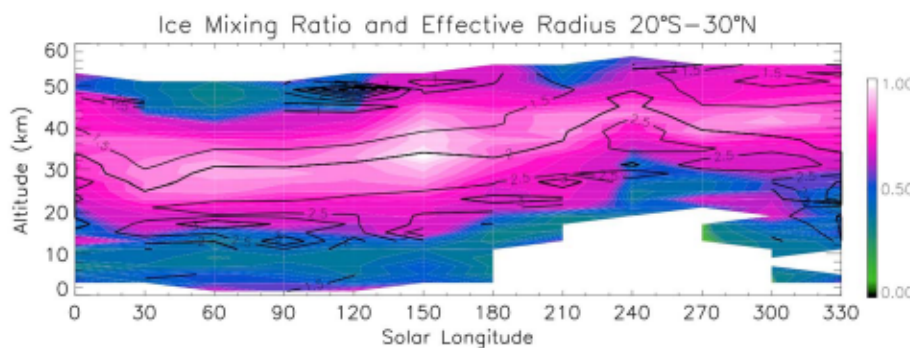


Figure 3. Zonal average Compact Reconnaissance Imaging Spectrometer for Mars water ice mixing ratio ($\Delta\tau/\Delta\text{mb}$, color shading) and effective radius (μm , black contours) in the 20°S – 30°N latitude region as a function of solar longitude and altitude.

particular altitude where the larger particles occur does vary with season. In all seasons, the largest particles at the bottom of the middle and lower latitude cloud layers have sizes $\geq 2.5 \mu\text{m}$ and often in excess of $3.0 \mu\text{m}$. The size of the particles within the cloud layer then trends downward with altitude reaching a typical minimum value of approximately $1.5 \mu\text{m}$.

The seasonal evolution of water ice cloud particle size in the polar regions (50 – 90° in each hemisphere) is more complicated. Guzewich et al. (2014) found that the polar hood clouds had roughly uniform particle sizes of $1.5 \mu\text{m}$. Our more complete seasonal record shows that the end of the polar hood cloud season in the northern hemisphere ($L_s = 330$ – 30°) does indeed exhibit fairly uniform ice particle size with altitude near $1.5 \mu\text{m}$, but the remainder of the observable year exhibits different behavior. In northern hemisphere spring and summer ($L_s = 30$ – 180°), clouds are relatively thin, and the highest ice mixing ratios (Figures 1 and 2) are near the surface and also at 25 – 40 -km altitude. In this season, the particles near the surface are generally small ($\leq 1.5 \mu\text{m}$), while the particles at higher altitudes are modestly larger in the 1.5 – $3.0 \mu\text{m}$ range. By the equinox, $L_s = 180^\circ$, clouds have become more abundant and thicker from 20 – 40 -km altitude, and they exhibit a strong sorting of particle size with altitude, similar to that seen in tropical latitudes. In the $L_s = 180$ – 210° period as the polar hood clouds are forming, the lower edge of the clouds near 20 km has particle sizes near $2.0 \mu\text{m}$ declining to less than $1 \mu\text{m}$ above 30 km. The difference in particle size between the initiation of the polar hood cloud and its dissipation suggests that the microphysical environment within the polar region changes as the fall and winter seasons progress, although the CRISM observations cannot directly inform us of the microphysical processes. Waugh et al. (2019) noted that the lower (0 – 20 km) winter polar atmosphere mixes with the lower latitude atmosphere on short (approximately tens of sols) timescales even during midwinter, suggesting that there should be a steady flux of ice nuclei (in the form of dust) into the polar atmosphere. Perhaps this effect, combined with the atmosphere mixing generated by CO_2 convection and precipitation (e.g., Hayne et al., 2012; Kuroda et al., 2013), serves to create an equilibrium in the polar atmosphere to create the fairly uniform $1.5\text{-}\mu\text{m}$ profile with altitude observed at the end of winter.

As stated above, we have less information about the south polar atmosphere but can note a few similarities with the north polar atmosphere. First, during the dissipation of the south polar hood clouds ($L_s = 150$ – 210°), the particle sizes are also generally near $1.5 \mu\text{m}$ (although the vertical profile is less complete than the north polar). Second, during late southern summer ($L_s = 270$ – 360°), there are thin clouds at high altitudes (35 – 50 km) that generally have larger particle sizes (2.0 – $3.5 \mu\text{m}$). We do not have enough information to compare the beginning of the polar hood cloud season in the southern hemisphere with that of the northern hemisphere.

We present the seasonal evolution (data were averaged into 30° bins of solar longitude) of water ice cloud particle size at tropical latitudes in more detail in Figures 3 and 4. Figures 3 and 4 average the 20°S – 30°N latitude range (roughly the range where the ACB clouds are most prevalent). The evolution of the ACB is more clearly seen in Figure 3, with an earlier secondary peak in water ice mixing ratio from $L_s = 60$ – 90° separated from the annual peak near $L_s = 150^\circ$ by a brief period where clouds are slightly less opaque

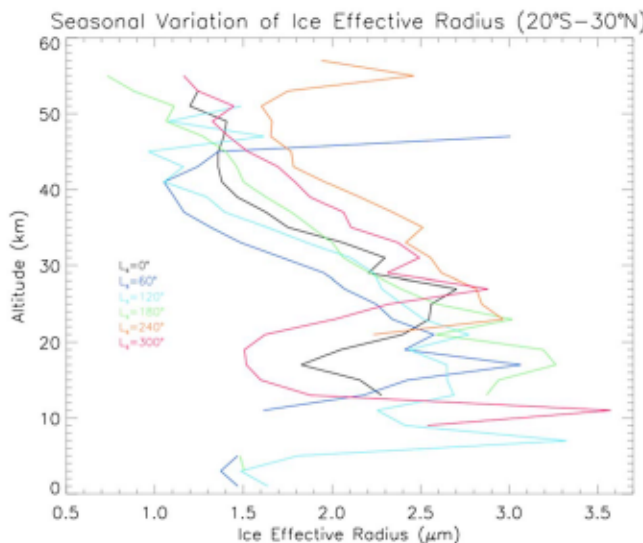


Figure 4. Zonal average Compact Reconnaissance Imaging Spectrometer for Mars water ice cloud effective radius (μm) in the 20°S – 30°N latitude region binned by 60° of solar longitude.

the availability of ice nuclei and the humidity) changes with altitude over the course of the year. Importantly, the peaks of water ice mixing ratio are distinctly separate from those of water ice particle size. This may suggest that continued condensation occurs as particles sediment through the cloud layer (e.g., Michelangeli et al., 1993).

In the early northern spring ($L_s = 30^{\circ}$) through late summer ($L_s = 150^{\circ}$), the largest particles ($>3.0 \mu\text{m}$) are below 20-km altitude. This region of particles $>3.0 \mu\text{m}$ slowly slopes upward with time in Figure 3 until it approaches 30 km near $L_s = 210^{\circ}$. At $L_s = 240^{\circ}$, the largest particles (now generally 2.5 – $3.0 \mu\text{m}$) are at 40 km. At that altitude, particles of that size will fall at rates of 1–10 km/sol (Kahre et al., 2008), suggesting they are constantly regenerated in situ (via advection of water vapor from the wetter southern hemisphere via the Hadley circulation; Montmessin et al., 2004) or maintained by consistent upward motion (e.g., as can occur along the slopes of the large Tharsis volcanoes; Rafkin, 2012). After $L_s = 240^{\circ}$, the altitude of the largest particles quickly drops back to near 25 km by $L_s = 0^{\circ}$. The different seasonal evolution of the water ice mixing ratio and the ice particle size vertical profiles implies that the processes that control each aspect of tropical clouds do not follow the same pattern through the year.

At the center of the tropical cloud layer, that is, the altitude with the highest ice mixing ratio (which changes with season as discussed above), the ice particle size varies by approximately $0.7 \mu\text{m}$ over the course of the year but generally is centered on a value of $1.9 \mu\text{m}$. At and near the equinoxes ($L_s = 0^{\circ}$ and 180°), the particle sizes at the center of the cloud are the smallest; in the range of 1.6 – $1.8 \mu\text{m}$. In the solstitial seasons ($L_s = 60$ – 150° and 210 – 300°), the particle sizes range from 1.9 – $2.3 \mu\text{m}$.

Figure 4 presents the data shown in Figure 3 in the form of a line plot and averages the data into bins of 60° of solar longitude (compared to 30° for the previous figures and again centered on the listed values) for the sake of clarity. The clearest altitude region with notable seasonal variation is between 30 and 45 km where ice cloud particles vary in size by up to $1.5 \mu\text{m}$ over the year. In all seasons, there is a steeply sloping curve to the ice particle size with altitude, but the curves are all offset from another in each season. The smallest particles at this altitude range are observed at $L_s = 60^{\circ}$ and then become larger through $L_s = 240^{\circ}$ before declining sharply at $L_s = 300^{\circ}$ and 0° . This is also seen in Figure 3.

From 10–25 km, the seasonal cycle is different with a maximum near $L_s = 180^{\circ}$ at over $3.0 \mu\text{m}$ that drops to near $1.5 \mu\text{m}$ at $L_s = 300^{\circ}$. The inflection point between these two altitude regions with differing seasonal cycles (25–30 km) typically marks the lower edge of the thicker cloud layer through much of the year, with the exception being after $L_s = 240^{\circ}$.

(Figure 17 of McCleese et al., 2010, hints at this as well). The timing of this brief decline in cloud opacity is aligned with the solstitial pause in dust storm activity described by many recent works (e.g., Guzewich et al., 2015, Lee et al., 2018, Lewis et al., 2016, Mulholland et al., 2016). The highest mixing ratios are also consistently near 30–35 km within the ACB, but the upper edge is extended up to 45–50 km at $L_s = 150$ – 180° (from 40 km earlier in the season). The lower edge of the cloud layer is near 20 km throughout the first half of the year. Indeed, the extension of the upper edge of the cloud layer near $L_s = 150^{\circ}$ appears to signal a step change in the altitude range where clouds are prevalent in the tropics. The lower boundary of the cloud layer similarly rises to near 30 km by $L_s = 240^{\circ}$, while the upper edge moves from 40–45 km to above 55 km. From $L_s = 180^{\circ}$ through the end of the year, the highest ice mixing ratios are generally above 40-km altitude and do not return to the 30-km altitude range until $L_s = 30^{\circ}$.

As seen in Figures 1 and 2, throughout the year, the tropical latitudes exhibit a strong sort of water ice cloud particle size with altitude with larger particles nearer the surface and smaller particles aloft. As described by Guzewich et al. (2014), this strongly implicates gravitational sedimentation is working to create this sorting effect. But the seasonal evolution shown in Figure 3 also shows that the microphysical environment (i.e.,

4. Discussion and Conclusion

We find that tropical clouds exhibit a strong sorting of water ice particle size with altitude at all seasons but with a clear seasonal cycle to the vertical profile of water ice particle size. The largest particles, at the bottom of the tropical cloud layer, are typically $>3.0\text{ }\mu\text{m}$ in size, declining to $<1.5\text{ }\mu\text{m}$ at the upper edge of the cloud layer in most seasons. At the altitude with maximum ice cloud mixing ratio, particles average $1.9\text{ }\mu\text{m}$ over the year, but with $0.7\text{ }\mu\text{m}$ of variation seasonally. This seasonal cycle does not precisely follow the seasonal cycle of water ice mixing ratio, suggesting that different processes (which are nevertheless linked) control the seasonal cycle of these two aspects of Martian tropical water clouds.

The seasonal evolution of north polar cloud ice particle size is more complex than initially suggested by Guzewich et al. (2014), with the vertical profile of ice particle size changing from one that is steeply sloped with altitude in the early autumn season ($L_s = 180\text{--}210^\circ$) to one that is uniform with altitude near $1.5\text{ }\mu\text{m}$ by the later winter and early spring ($L_s = 330\text{--}30^\circ$). This implies seasonally changing microphysical conditions within the northern hemisphere winter polar vortex, possibly controlled by processes such as the time-variable influx of dust and CO_2 condensation and precipitation events.

The CRISM observations alone cannot directly inform us of those processes, but in conjunction with other data, we can begin to disentangle competing effects of ice nuclei (i.e., dust) abundance and water vapor saturation. There is now a large record of limb profile of atmospheric dust from instruments such as the Mars Climate Sounder, Thermal Emission Spectrometer, and Spectroscopy for Investigation of Characteristics of the Atmosphere of Mars (SPICAM), as well as CRISM, so we know with good fidelity the abundance of ice nuclei. There is far less information about the vertical distribution of water vapor and more data on this crucial variable is desperately needed. Montmessin et al. (2017) provides an overview of SPICAM's occultation measurements of the water vapor profile. The vertical motion of the hygropause with season shown by Montmessin et al. (2017) reasonably follows our CRISM retrievals of water ice mixing ratio, where clouds move to higher altitudes in the warmer and dustier southern spring and summer ($L_s = 180\text{--}270^\circ$) seasons. Observations of water vapor supersaturation with SPICAM (Maltagliati et al., 2011) suggest that the balance between water vapor and ice nuclei abundance occasionally can favor water vapor, which would encourage larger ice particles assuming all else is equal.

This work represents the first climatology of the vertical distribution of Martian water ice cloud particle sizes and extends the work of Guzewich et al. (2014) with more complete seasonal and multiyear coverage. The size of water ice cloud particles are important for understanding how they interact with solar radiation and thus how they impact the Martian climate. These data represent an important guide for Mars GCMs to improve their cloud microphysical routines to better match observations of Martian atmospheric temperatures and aerosol distributions.

Acknowledgments

M.D. Smith was supported as a member of the CRISM science team. We thank Franck Montmessin and Nicholas Heavens for helpful reviews. All CRISM retrievals used in this work are included in supporting information.

References

- Clancy, R. T., Sandor, B. J., Wolff, M. J., Christensen, P. R., Smith, M. D., Pearl, J. C., et al. (2000). An intercomparison of ground-based millimeter, MGS TES, and Viking atmospheric temperature measurements: Seasonal and interannual variability of temperatures and dust loading in the global Mars atmosphere. *Journal of Geophysical Research*, *105*(E4), 9553–9571. <https://doi.org/10.1029/1999JE001089>
- Clancy, R. T., Wolff, M. J., & Christensen, P. R. (2003). Mars aerosol studies with the MGS-TES emission phase function observations: Optical depths, particle sizes, and ice cloud types versus latitude and solar longitude. *Journal of Geophysical Research*, *108*(E9), 5098. <https://doi.org/10.1029/2003JE002058>
- Guzewich, S. D., Smith, M. D., & Wolff, M. J. (2014). The vertical distribution of Martian aerosol particle size. *Journal of Geophysical Research: Planets*, *119*, 2694–2708. <https://doi.org/10.1002/2014JE004704>
- Guzewich, S. D., Talaat, E. R., Toigo, A. D., Waugh, D. W., & McConnochie, T. H. (2013). High-altitude dust layers on Mars: Observations with the Thermal Emission Spectrometer. *Journal of Geophysical Research: Planets*, *118*, 1177–1194. <https://doi.org/10.1002/jgre.20076>
- Guzewich, S. D., Toigo, A. D., Kulowski, L., & Wang, H. (2015). Mars Orbiter Camera climatology of textured dust storms. *Icarus*, *258*, 1–13. <https://doi.org/10.1016/j.icarus.2015.06.023>
- Hayne, P. O., Paige, D. A., Schofield, J. T., Kass, D. M., Kleinböhl, A., Heavens, N. G., & McCleese, D. J. (2012). Carbon dioxide snow clouds on Mars: South polar winter observations by the Mars Climate Sounder. *Journal of Geophysical Research*, *117*, E08014. <https://doi.org/10.1029/2011JE004040>
- Heavens, N. G., Benson, J. L., Kass, D. M., Kleinböhl, A., Abdou, W. A., McCleese, D. J., et al. (2010). Water ice clouds over the Martian tropics during northern summer. *Geophysical Research Letters*, *37*, L18202. <https://doi.org/10.1029/2010GL044610>
- Hoyle, C. R., Luo, B. P., & Peter, T. (2005). The origin of high ice crystal number densities in cirrus clouds. *Journal of the Atmospheric Sciences*, *62*(7), 2568–2579. <https://doi.org/10.1175/JAS3487.1>
- Kahre, M. A., Hollingsworth, J. L., Haberk, R. M., & Murphy, J. R. (2008). Investigations of the variability of dust particle sizes in the Martian atmosphere using the NASA Ames general circulation model. *Icarus*, *195*(2), 576–597. <https://doi.org/10.1016/j.icarus.2008.01.023>

- Kahre, M. A., Hollingsworth, J. L., Haberle, R. M., & Wilson, R. J. (2015). Coupling the Mars dust and water cycles: The importance of radiative-dynamic feedbacks during northern hemisphere summer. *Icarus*, 260, 477–480. <https://doi.org/10.1016/j.icarus.2014.07.017>
- Kokhanovsky, A. (2004). Optical properties of terrestrial clouds. *Earth-Science Reviews*, 64(3–4), 189–241. [https://doi.org/10.1016/S0012-8252\(03\)00042-4](https://doi.org/10.1016/S0012-8252(03)00042-4)
- Kuroda, T., Medvedev, A. S., Kasaba, Y., & Hartogh, P. (2013). Carbon dioxide ice clouds, snowfalls, and baroclinic waves in the northern winter polar atmosphere of Mars. *Geophysical Research Letters*, 40, 1484–1488. <https://doi.org/10.1002/grl.50326>
- Lee, C., Richardson, M. I., Newman, C. E., & Mischna, M. A. (2018). The sensitivity of solsticial pauses to atmospheric ice and dust in the MarsWRF general circulation model. *Icarus*, 311, 23–34. <https://doi.org/10.1016/j.icarus.2018.03.019>
- Lewis, S. R., Mulholland, D. P., Read, P. L., Montabone, L., Wilson, R. J., & Smith, M. D. (2016). The solsticial pause on Mars: 1. A planetary wave reanalysis. *Icarus*, 264, 456–464. <https://doi.org/10.1016/j.icarus.2015.08.039>
- Madeleine, J.-B., Forget, F., Millour, E., Navarro, T., & Spiga, A. (2012). The influence of radiatively active water ice clouds on the Martian climate. *Geophysical Research Letters*, 39, L23202. <https://doi.org/10.1029/2012GL053564>
- Maltagliati, L., Montmessin, F., Fedorova, A., Korablev, O., Forget, F., & Bertaux, J.-L. (2011). Evidence of water vapor in excess of saturation in the atmosphere of Mars. *Science*, 333(6051), 1868–1871. <https://doi.org/10.1126/science.1207957>
- McCleese, D. J., Heavens, N. G., Schofield, J. T., Abdou, W. A., Bandfield, J. L., Calcutt, S. B., et al. (2010). Structure and dynamics of the Martian lower and middle atmosphere as observed by the Mars Climate Sounder: Seasonal variations in zonal mean temperature, dust, and water ice aerosols. *Journal of Geophysical Research*, 115, E12016. <https://doi.org/10.1029/2010JE003677>
- Michelangeli, D. V., Toon, O. B., Haberle, R. M., & Pollack, J. B. (1993). Simulations of the formation and evolution of water ice clouds in the Martian atmosphere. *Icarus*, 100, 261–285.
- Montmessin, F., Forget, F., Rannou, P., Cabane, M., & Haberle, R. M. (2004). Origin and role of water ice clouds in the Martian water cycle as inferred from a general circulation model. *Journal of Geophysical Research*, 109, E10004. <https://doi.org/10.1029/2004JE002284>
- Montmessin, F., Korablev, O., Lefèvre, F., Bertaux, J.-L., Fedorova, A., Trokhimovskiy, A., et al. (2017). SPICAM on Mars Express: A 10 year in-depth survey of the Martian atmosphere. *Icarus*, 297, 195–216. <https://doi.org/10.1016/j.icarus.2017.06.022>
- Mulholland, D. P., Lewis, S. R., Read, P. L., Madeleine, J.-B., & Forget, F. (2016). The solsticial pause on Mars: 2 modelling and investigation of causes. *Icarus*, 264, 465–477. <https://doi.org/10.1016/j.icarus.2015.08.038>
- Murchie, S., Arvidson, R., Bedini, P., Beisser, K., Bibring, J.-P., Bishop, J., et al. (2007). Compact Reconnaissance Imaging Spectrometer for Mars (CRISM) on Mars Reconnaissance Orbiter (MRO). *Journal of Geophysical Research*, 112, E05S03. <https://doi.org/10.1029/2006JE002682>
- Navarro, T., Forget, F., Millour, E., Greybush, S. J., Kalnay, E., & Miyoshi, T. (2017). The challenge of atmospheric data assimilation on Mars. *Earth and Space Science*, 4, 690–722. <https://doi.org/10.1002/2017EA000274>
- Navarro, T., Madeleine, J.-B., Forget, F., Spiga, A., Millour, E., Montmessin, F., & Määttänen, A. (2014). Global climate modeling of the Martian water cycle with improved microphysics and radiatively active water ice clouds. *Journal of Geophysical Research: Planets*, 119, 1479–1495. <https://doi.org/10.1002/2013JE004550>
- Pearl, J. C., Smith, M. D., Conrath, B. J., Bandfield, J. L., & Christensen, P. R. (2001). Observations of Martian ice clouds by the Mars Global Surveyor Thermal Emission Spectrometer: The first Martian year. *Journal of Geophysical Research*, 106(E6), 12,325–12,338. <https://doi.org/10.1029/1999JE001233>
- Petty, G. W. (2006). *A first course in atmospheric radiation* (2nd ed.). Madison, WI: Sundog Publishing.
- Pottier, A., Forget, F., Montmessin, F., Navarro, T., Spiga, A., Millour, E., et al. (2017). Unraveling the Martian water cycle with high-resolution global climate simulations. *Icarus*, 291, 82–106. <https://doi.org/10.1016/j.icarus.2017.02.016>
- Rafkin, S. C. R. (2012). The potential importance of non-local, deep transport on the energetics, momentum, chemistry, and aerosol distributions in the atmospheres of Earth, Mars, and Titan. *Planetary and Space Science*, 60(1), 147–154. <https://doi.org/10.1016/j.pss.2011.07.015>
- Shaposhnikov, D. S., Rodin, A. V., Medvedev, A. S., Fedorova, A. A., Kuroda, T., & Hartogh, P. (2018). Modeling the hydrological cycle in the atmosphere of Mars: Influence of a bimodal size distribution of aerosol nucleation particles. *Journal of Geophysical Research: Planets*, 123, 508–526. <https://doi.org/10.1002/2017JE005384>
- Smith, M. D. (2004). Interannual variability in TES atmospheric observations of Mars during 1999–2003. *Icarus*, 167(1), 148–165. <https://doi.org/10.1016/j.icarus.2003.09.010>
- Smith, M. D. (2009). THEMIS observations of Mars aerosol optical depth from 2002–2008. *Icarus*, 202(2), 444–452. <https://doi.org/10.1016/j.icarus.2009.03.027>
- Smith, M. D., Wolff, M. J., Clancy, R. T., Kleinböhl, A., & Murchie, S. L. (2013). Vertical distribution of dust and water ice aerosols from CRISM limb-geometry observations. *Journal of Geophysical Research: Planets*, 118, 321–334. <https://doi.org/10.1002/jgre.20047>
- Steele, L. J., Lewis, S. R., & Patel, M. R. (2014). The radiative impact of water ice clouds from a reanalysis of Mars Climate Sounder data. *Geophysical Research Letters*, 41, 4471–4478. <https://doi.org/10.1002/2014GL060235>
- Warren, S. (1984). Optical constants of ice from the ultraviolet to the microwave. *Applied Optics*, 23(8), 1206–1225. <https://doi.org/10.1364/AO.23.001206>
- Waugh, D. W., Toigo, A. D., & Guzewich, S. D. (2019). Age of Martian air: Time scales for Martian atmospheric transport. *Icarus*, 317, 148–157. <https://doi.org/10.1016/j.icarus.2018.08.002>
- Wilson, R. J., & Guzewich, S. D. (2014). Influence of water ice clouds on nighttime tropical temperature structure as seen by the Mars Climate Sounder. *Geophysical Research Letters*, 41, 3375–3381. <https://doi.org/10.1002/2014GL060086>
- Wilson, R. J., Lewis, S. R., Montabone, L., & Smith, M. D. (2008). Influence of water ice clouds on Martian tropical atmospheric temperatures. *Geophysical Research Letters*, 35, L07202. <https://doi.org/10.1029/2007GL032405>
- Wilson, R. J., Neumann, G. A., & Smith, M. D. (2007). Diurnal variation and radiative influence of Martian water ice clouds. *Geophysical Research Letters*, 34, L02710. <https://doi.org/10.1029/2006GL027976>
- Wiscombe, W. J. (1996). *Mie scattering: Advances in technique and fast, vector speed computer codes*, NCAR/TN-140+STR. Boulder, CO: Natl. Cent. For Atm. Res.
- Wolff, M. J., Clancy, R. T., Smith, M. D., Arvidson, R., Kahre, M., SeeLOS, F. IV, & Morris, R. V. (2009). Wavelength dependence of dust aerosol single scattering albedo as observed by CRISM. *Journal of Geophysical Research*, 114, E00D04. <https://doi.org/10.1029/2009JE003350>